

Inspecting Marquetries at Different Wavelengths: The Preliminary Numerical Approach as Aid for a Wide-Range of Non-destructive Tests

S. Sfarra¹ · P. Theodorakeas² · J. Černecký³ · E. Pivarčiová³ · S. Perilli¹ · M. Kouř²

Received: 9 January 2016 / Accepted: 29 November 2016 / Published online: 19 December 2016
© Springer Science+Business Media New York 2016

Abstract The present study is based on the non-destructive inspection of two marquetries representing arms' coats, which were produced by the Technical University in Zvolen (Slovakia) and tested under laboratory conditions. The aforementioned samples were made of traditional European and exotic wood species, while the veneers of the decorative layers were prepared through the technology cutting technique, emphasizing in such a manner the wooden texture. One sample was a defect-free panel, while the second one consisted of three sub-superficial flaws and one superficial putty insert, added during the manufacturing stage. The samples were inspected by different non-destructive techniques, such as visible imaging, ultraviolet testing, near-infrared reflectography and transmittography, infrared thermography, holographic interferometry, digital image correlation, laser speckle contrast imaging and ultrasonic testing. Sometimes a comparison was not performed, by avoiding unnecessary data processing. Numerical simulations focusing on the optimization of the provided thermal flux anticipated the experimental results. The latter analysis proved the necessity for the inte-

gration of experimental and numerical testing in similar case studies. A peculiarity of this work is the additional creation of an ad hoc Matlab[®] code, written under the LSCI conditions, which identifies the wooden texture. The interactive methodology applied in the present study verified the synergy of the selected inspection methods enabling the production of a complete view for the preservation state of the inspected marquetry samples, through the comparison and/or the correlation of the individual informative content produced by each inspection procedure.

Keywords Marquetry · Wood · Non-destructive testing techniques · Numerical simulation · Flaw · Manufacturing Process

1 Introduction

On one hand, the word *intarsia* is derived from the Latin *interserere*, to insert, according to the best Italian authorities. On the other hand, *marquetry* is a word of much later origin, and comes from the French *marquetrier*, to mark. Therefore, it seems accurate to apply the former term to these inlays of wood, at which a space is first sunk in the solid and afterwards filled with a piece of wood, cut to fit it. The use of the latter term has been adapted to describe the modern practice of cutting, where several sheets of differently-colored thin wood are placed together to the same design, so that eight or ten copies of different colors may be produced by one cutting. In such a manner, each wooden sheet is fitted to each other through subsequent arranging and gluing [1–3]. The most commonly used materials in such constructions are veneer plywood, which have variegated texture. The term plywood is usually referred to sheets or boards that are made from three or more odd numbers of thin layers of wood—known as wood

✉ S. Sfarra
stefano.sfarra@univaq.it

¹ Las.E.R. Laboratory, Department of Industrial and Information Engineering and Economics, University of L'Aquila, Piazzale E. Pontieri no. 1, 67100 L'Aquila (AQ), Monteluco di Roio, Italy

² NDT Lab, Materials Science & Engineering Department, School of Chemical Engineering, National Technical University of Athens, Iroon Polytechniou 9, 157 80 Zografou, Athens, Greece

³ Faculty of Environmental and Technology Manufacturing, Technical University in Zvolen, Ul. T.G. Masaryka 2117/24, 960 53 Zvolen, Slovakia

veneers. Usually, the grains and/or the knots, etc. are used in the overall effect of the picture during the planning procedure. However, most of these flaws have some detrimental effects on the tree, e.g., lower its market value. The restoration phase of this type of objects must be anticipated by an in-depth knowledge of the typical correlated flaws [4]. The design of a methodology for the quality evaluation of the coating of woods and of special wood products, through the aid of non-destructive optical methods, have been recently studied [5].

Based on the aforesaid, the main objective of this work was to conduct a comparative study by means of non-destructive testing (NDT) in order to detect and monitor common defects presented on marquetry panels. For that purpose, a sample containing two different types of simulated flaws: the honeycombing (i.e., parting of the grain internally) and the resin (pitch) pocket effects (i.e., an opening having the saucer shape of a growth ring which is followed by resin accumulation and may appears as a resinous streak on the surface of timber) was inspected by different non invasive methods. More specifically, a methodology was adapted, on which the defective sample was subjected to imaging tests at different wavelengths (ultraviolet, near-infrared, and long-infrared) and illuminated by two different lasers also working at different wavelengths (532 and 632 nm) during the implementation of the holographic interferometry (HI) and the digital image correlation (DIC) tests. Last, the wooden sample was also inspected by means of ultrasonic testing (UT). In such a manner different informative contents, derived by different testing procedures, were correlated in order to produce an effective monitoring tool of such wooden objects. Nevertheless, as these constructions generally have a composite and heterogeneous nature, initially Comsol[®] Multiphysics computer program was used in order to establish the optimum heat flux to be provided on the front side of the sample, a useful information for the definition of the experimental parameters in thermographic testing. The numerical analysis, taking into account the very complex external design of the inspected surface, i.e., a coat of arms of the Italian Republic, required an innovative expedient in order to preserve the real geometry. Indeed, the shape was imported into Comsol[®] Multiphysics thanks to the use of Photoshop[®] computer program. From the above described approach, the grain of the external sheets in wood was also inspected. Grain refers to the direction of the main elements of the wood. The manner in which grain appears will depend upon one or more of the following: (a) the direction of the cut, (b) the location of the cut, (c) the condition of the wood, and (d) the arrangement of the wood cells.

To the best of the authors' knowledge, this is the first time that a marquetry reproduction has been inspected in such a detailed manner, as indicated by previous analytical experiences [6–9].

2 Materials and Methods

2.1 Description of the Marquetry Defective Sample

The main characteristics of the inspected sample are reported in Fig. 1. In particular, the middle layer is constituted by MDF (medium-density fiberboard) of 3 mm thickness, while the substratum and the top decorative layers are constituted by maple wood having thicknesses of 0.3 and 0.6 mm, respectively. In addition, mahogany, maple, wenge, walnut (both the core and the whitish parts) woods were used in order to complete the coat of arms. Instead, the flaws were designed as follows: **A**—a void crossing the topmost layers of the MDF material, **B**—a void crossing the MDF material, **C**—a void crossing the deepest layers of the MDF material, and **D**—a putty insert. The top layer (**1**) having a decorative role was made by a combination of light and dark veneers coming from European and exotic countries. It has a thickness of 0.6–0.7 mm, while the bottom layer made of maple veneer has a thickness of 0.7 mm. The maple, mahogany, walnut, wenge woods were smoothed using a band grinding machine in order to produce a flat surface.

The decorative layer was cut by a CO₂ laser according to a dedicated software. During the cutting process, a charred area occurred as can be seen from the irregular dark borderline in Fig. 2 (see area **C** in Fig. 2) [10].

Laser cut veneers were assembled together part by part into a final marquetry, named *the coat of arms of the Italian Republic*. The marquetry was glued by a polyvinyl acetate based glue and pressed for 24 h. In order to fill in the cut crevices arose during the cutting process, two-part polyester putty with a high content of cellulose (wood powder) was used. This putty has been easily finished by sandpaper; it

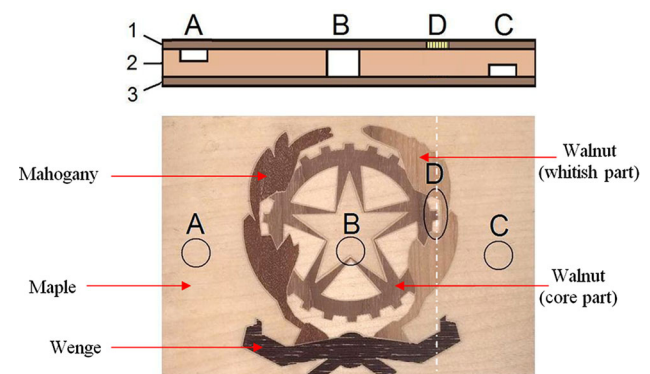


Fig. 1 Marquetry. Schematization of the coat of arms of the Italian Republic made by various veneers: *1* marquetry, *2* MDF board and position of the flaws along the *z* axis, *3* veneer (maple wood). **A**, **B**, **C**—flaws (simulating the honeycombing effect) included into the sample at the manufacturing stage, **D**—putty [simulating the resin (pitch) pocket effect]

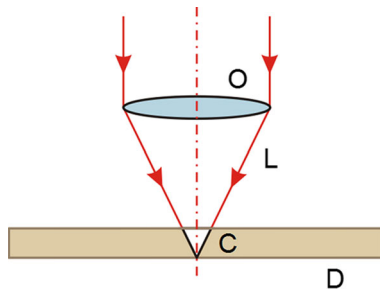


Fig. 2 Laser cutting for marquetry production. **O** objective, **L** laser ray, **D** veneer, and **C** charred part with carbon content

reacted with the changes of the environmental conditions (temperature and relative humidity), and it does not sink. Therefore, the heat energy was supplied by the laser beam which permitted a free-machining tool steels.

2.2 Nondestructive Testing (NDT) Techniques

From now on, the article is divided into four main parts; these offer theoretical background about the sensing techniques, the description of the approach in which the sample has been both stimulated and analyzed by a numerical simulation realized in Comsol[®] Multiphysics, the discussion on the main findings and finally the conclusions derived from this study.

2.2.1 Holographic Interferometry (HI) Technique

HI can visualize the variation between different deformation states of an opaque surface. HI produces interference between two or more waves, at least one of which is reconstructed by a hologram. In particular, the BS (Fig. 3) “produces” two set of waves. The first one, called *object beam*, is scattered by the marquetry sample, while the second one is termed the *reference beam*. In the present case, holograms were recorded thanks to a photo-thermoplastic based plate, usually named as holographic plate (HP), while the final interferogram was imaged by a high resolution photocalera (CCD).

In order to change the deformation state between the generation of two optical wave fields that have to be compared, the object must be loaded, or an applied load must be varied [11, 12]. In the HI field, it is possible to investigate and measure how an object deforms in reaction to a specific load. In Fig. 3, the load is a thermal stress provoked by a heat source (HS item in the schematic).

Therefore, one has to decide on the proper loading which comprises the type, the direction, and the amplitude of the load. Five basic types of loading play a dominant role: direct mechanical load, pressure load, vibrational load, impulse

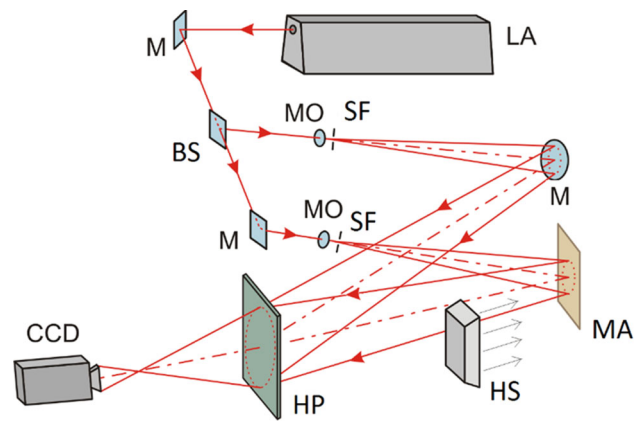


Fig. 3 Holographic set up. **LA** laser ($\lambda = 632 \text{ nm}$), **CCD** camera, **M** mirror, **BS** beam splitter, **MO** micro-objective lens, **SF** spatial filter, **MA** marquetry, **HP** holographic plate, **HS** heat source

load, and thermal load. In particular, there is a number of ways to apply thermal load: radiation sources like IR-lamps may heat the tested component—often from the rear side of the inspected surface—hot air jets may be generated by conventional hair-dryers, volatile fluids sprayed on a surface which cool it during evaporation, or by high power DC generating heat in conductive material. Similarly, heat may be brought to a component by induction heating or by microwaves, especially to materials containing water. Due to thermal expansion most materials are deformed when the temperature is changed. Furthermore, the thermal conductivity locally varies at voids like the sub-superficial flaws presented herein. The authors chosen this type of stress according to previous experiences in the matter [13–15] with a minor modification. The lamps have been substituted by a ceramic infrared radiation source of 150 W power, that seems to provide a more uniform heating phase. The temperature amplitude with respect to the steady-state has been set at $\Delta T = 0.8^\circ\text{C}$.

In this work, the HI double-exposure (DE) method was used; it permanently keeps information about the changes of the object state. In particular, the decorated surface was illuminated twice by LA, separated by a fixed time interval. Both holograms (i.e., the holograms recorded before and after the unperceivable deformation caused by the induced variation in temperature) were stored on the same holographic plate. During reconstruction, the two images interfere as though there were two copies of the object present. Where the displacement between the two “copies” is such that the reflected light would be shifted by an integral multiple of half wavelengths there will be a dark fringe in the combined image. Conversely, bright fringes occur when the displacement is an integral number of wavelengths [16]. The geometry is shown in Fig. 4.

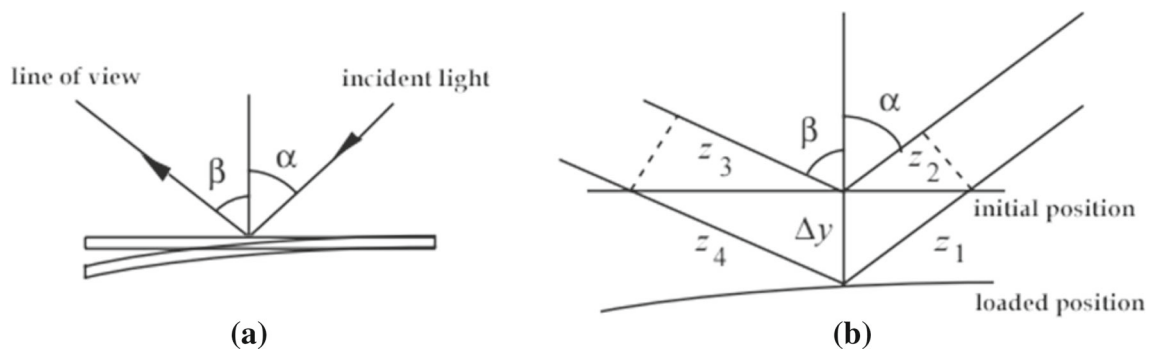


Fig. 4 **a** Geometry during reconstruction of the DE hologram, and **b** an enlarged view of a portion of a plate, showing the displacement in more detail

The change in optical path length ΔO due to the shift in position Δy of the surface is:

$$\Delta O = (z_1 + z_4) - (z_2 + z_3) \quad (1)$$

Using the given angles this becomes:

$$\Delta O = \Delta y (\cos \alpha + \cos \beta) \quad (2)$$

The condition for interference can be written as:

$$\Delta O = \frac{n \lambda}{2} \quad (3)$$

where, odd integers imply dark fringes and even integers imply bright fringes. Equating these two expressions, the formula concerning the determination of Δy is:

$$\Delta y = \frac{n \lambda}{2 (\cos \alpha + \cos \beta)} \quad (4)$$

where, n counts both dark and light fringes from some undeflected reference point. The holographic plate is then developed and reconstructed in order to observe and record the interference pattern which is superimposed on the object.

Internal flaws (splitting, voids, wrong gluing, air bubbles, etc.) that occurred inside multi-layer materials and are not visible to the naked eye, can be detected as they conduct the induced heat in a different manner than the defect-free areas. In addition, these flaws are revealed by the interference fringes during a sudden modification of the local mechanical properties. This effect is shown in Sect. 3.

2.2.2 Imaging Methods

All images were collected using a CANON 40DH camera *spectrum enhanced*, which was modified after removing the inbuilt UV-IR blocking filter and adding the Idas Clear/AR filter. This allowed the full sensitivity range of the CMOS

(22.2×14.8 mm at 10 megapixels— $5.7 \mu\text{m}$ pixel pitch) sensor (ca. 300–1000 nm) to be used. The used lens was a Canon EF55-200, while the camera was equipped with an internal filter named EOS045. The wavelength ranges required for the applications subsequently explained, have been selected by placing a filter in front of the lens.

2.2.2.1 Visible Imaging (VI) Illumination was provided by two Philips IR 250S lamps equipped with softbox diffusers, which were positioned symmetrically at approximately 30° with respect to the focal axis of the camera. This produced a considerable amount of infrared and visible radiation, while the UV component was negligible. An interference UV-IR blocking filter IDAS-UIBAR filter (bandpass, ca. 380–700) was placed in front of the lens.

2.2.2.2 Ultraviolet Testing (UVT) The radiation source used for the UV test was consisted of two sets of LED_s lamps, while the camera was equipped with an interference filter (band-pass, ca. 360 nm). The emission of the radiation source is a relatively sharp line centered at 360 nm. The radiation sources were symmetrically positioned at approximately 30° with respect to the focal axis of the camera.

2.2.2.3 Near-Infrared Reflectography (NIRR) and Transmittography (NIRT) The light sources used for NIRR and NIRT techniques were identical to those used for the generation of visible-reflected light. Nevertheless, the camera used for the relevant testing was equipped with a series of different band-pass filters mounted on the lens and working at 680, 715, 760, 850, 950, and 1000 nm. In reflection mode, the respective positions of the lamps were the same as in the case of the visible imaging inspection, while in transmission mode, only one lamp positioned along the perpendicular ideal axis passing through the sample's center was used. The NIR measurements have been integrated by also working with two different LED_s lamps set at 850 and 940 nm, respectively. The experimental setup is shown in Fig. 4.

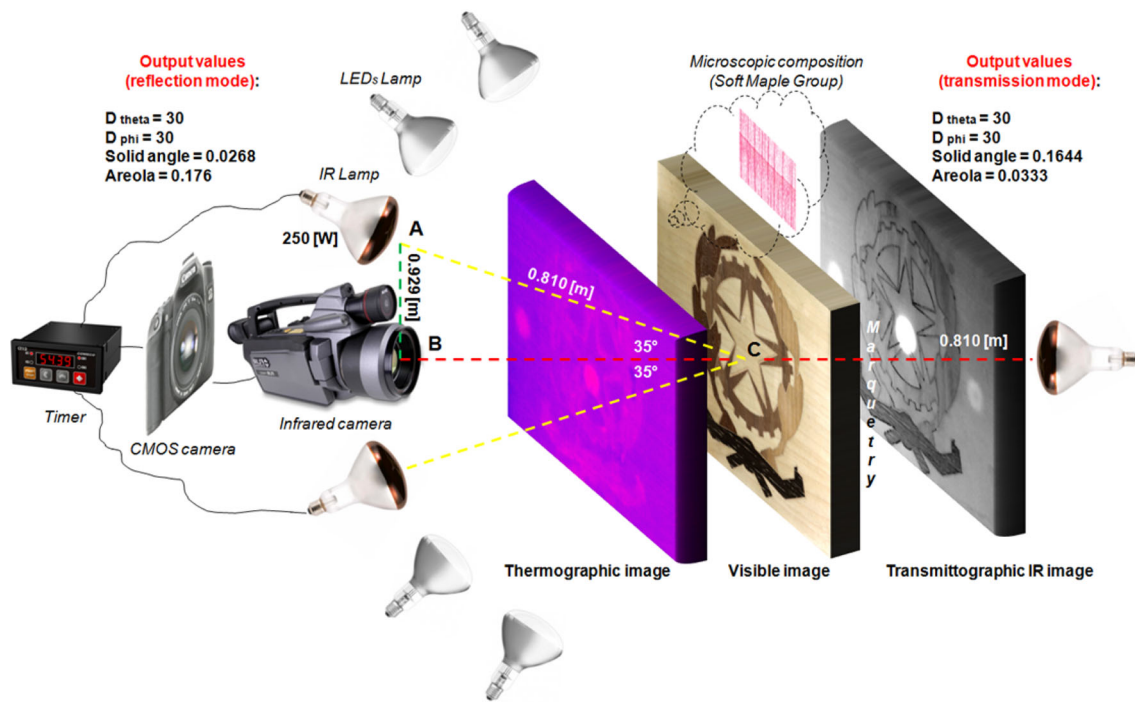


Fig. 5 VI, UVT, NIRR, NIRT and IRT experimental setup, the main parameters for the computation of the emitted heat flux, and output values from the Matlab® script (Color figure online)

2.2.3 Infrared Thermography (IRT) Technique

Each object having a temperature higher than the absolute zero emits irradiative energy in the infrared portion of the electromagnetic spectrum, which can be detected through the aid of specialized infrared detectors; the emitted energy is proportional to its temperature. In this work, active IRT has been carried out by applying a thermal stimulation on the marquetrys and monitoring their surface temperature variation during the transient heating and cooling phases. The analysis involves heat conduction in solids [17], while the experimental raw thermograms have been acquired through square pulse thermography (SPT) method, working in reflection mode (Fig. 5).

Since the numerical simulations were propaedeutic for the thermographic measurement, at this point it is important to introduce the main technical physics concepts related to the key elements used during the experimental evaluation. Indeed, the heating and cooling of a body with changes in temperature represent non-steady-state processes of thermal transfer. The rate of heating or cooling depends on the dimension and geometry of the object, specifically, the relationship between surface area and volume, known as the “form factor”. It has been experimentally and theoretically demonstrated that the greater this value is, the faster the propagation of heat in these processes becomes [18]. Additionally, the study of different objects with diverse geometrical forms has revealed that the temperature of an object, during heat-

ing or cooling, is increasing or decreasing exponentially. In both cases, three stages can be identified: an irregular thermal regime where the temperature at each point and the speed at which it varies over time depend fundamentally on the initial temperature distribution. After a certain period of time, a second stage begins: the regular thermal regime. During this period, the influence of the initial condition declines, and the process is determined principally by the heat transfer coefficient of the surface, the dimensions and shape of the body, as well as its physical properties. During this phase, there is a regular thermal regime and the laws of the variation in the temperature field over time take the following universal and simple form [18]:

$$\ln \vartheta = -m \cdot t + C \tag{5}$$

where, ϑ is the excess temperature, t is time, C is a constant and m is the rate of heating or cooling, that is:

$$\vartheta = C e^{-m \cdot t} \tag{6}$$

It is during this period that the variation in the excess temperature has the exponential character mentioned above. There is a linear variation in the logarithm of the excess temperature; the value m is constant and it does not depend on the position or time. This is called *the rate of heating or cooling* and determines the speed at which a body heats up or cools down. This regularization of the temperature field is

Table 1 Experimental equipment and acquisition parameters for the inspection of the marquetry

Las.E.R. Lab. (University of L'Aquila)—Italy		
Experimental equipment	Acquisition parameters	
Thermal stimulation	Sampling rate, f_s	1 Hz
IR lamps of 250 W power each	Acquisition duration, t_{acq}	210 s + 1 s (cold image)
Heating duration: 60 s		60 s heating + 150 s cooling
Monitoring of cooling phase: 150 s	Time interval, $\Delta t = 1/f_s$	1 s
Thermographic monitoring:	Total number of frames	211 (60 frames heating + 150 frames cooling + 1 cold image)
FLIR ThermaCAM S65 HS, Focal Plane Array, long wave, 320×240 pixels		
NDT Lab. (National Technical University of Athens)—Greece		
Experimental equipment	Acquisition parameters	
Thermal stimulation	Sampling rate, f_s	15 Hz
Halogen lamps of 500 W power each	Acquisition duration, t_{acq}	60 s
Heating duration: 15 s		15 s heating + 45 s cooling
Monitoring of cooling phase: 45 s	Time interval, $\Delta t = 1/f_s$	0.0667 s
Thermographic monitoring:	Total number of frames	900 (225 frames heating + 675 frames cooling)
FLIR ThermaCAM SC640, Focal Plane Array, long wave, 640×480 pixels		

general and common to all types of bodies whether they are homogeneous or heterogeneous. In the third and final stage, the temperature of the entire body coincides with that of the environment in which it is located, reaching thermal equilibrium and passing from a non-steady state to a steady state [19].

The measurements have been conducted both in the Las.E.R. Lab. from the University of L'Aquila (Italy), and in the NDT Lab from National Technical University of Athens (Greece). During the tests, two lamps (250 W power each in the first case—IR, and 500 W power each in the second case—halogen), as well as two different thermal cameras (8–14 μm) by FLIR (320×240 pixels in the first case, and 640×480 pixels in the second case), have been used. The selected experimental parameters are presented in Table 1.

The acquired thermal dataset has a 3D format, measuring the 2D surface temperature distribution (thermal images) as a function of time t . Therefore, the entire dataset can be expressed as $T(x, y, t)$ where T is the temperature on the surface position (x, y) . The sequence retrieved from the above experimental procedure was processed in the *Matlab*[®] environment, using the open source *IR View* graphical user interface, developed and released by the Computer Vision and Systems Laboratory (CVSL) of Université Laval [20]. In particular, the acquired data were analyzed after studying the whole sequence of images including both the heating up and cooling down phases. The post processing algorithms applied in order to enhance both the image quality and the flaw detectability of the raw thermal data were thermographic

signal reconstruction (TSR) [21] and principal component thermography (PCT) [22].

TSR algorithm is based on the assumption that the temperature profiles for non-defective areas, which are following the decay curve given by the one-dimensional solution of the Fourier diffusion equation, can be rewritten in the logarithmic notation and further expanded into a polynomial series. Once the time evolution data has been approximated into a polynomial series, the original temperature data can be reconstructed in order to produce synthetic temperature data and derivative images, which offer a higher degree of signal to noise ratio, spatial and temporal resolution increase and a further reduction of data to be manipulated. Even that first, second or higher order derivative images can be created, in practice only the first and second time-derivative images are used providing information on the rate of temperature variation.

PCT extracts the image features and reduces undesirable signals. It relies on singular value decomposition (SVD), which is a tool to extract spatial and temporal data from a matrix in a compact manner, as it projects the original data onto a system of orthogonal components known as empirical orthogonal functions (EOF). The 1st EOF on the transformed matrix represents the most important characteristic variability of the data; the 2nd EOF contains the second most important variability, and so on [22]. Usually, original data can be adequately represented with only a few EOFs, as typically, a sequence of 1000 thermal images can be replaced by 10 or less EOFs.

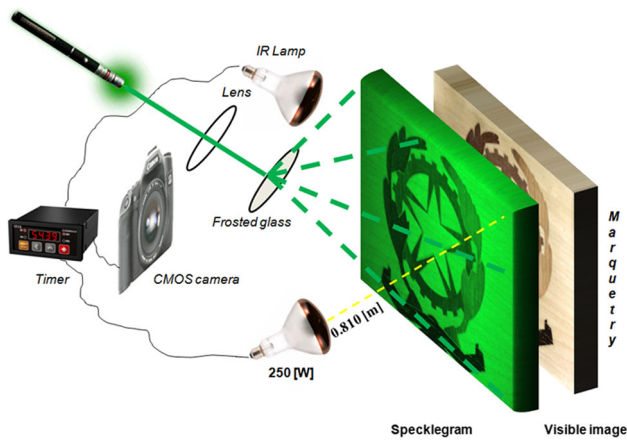


Fig. 6 DIC and LSCI experimental setup

2.2.4 Digital Image Correlation (DIC) Technique

In two-dimensional DIC technique, the displacements are directly detected from digital images of the object surface (marquetry). Figure 6 shows the experimental setup for the DIC measurements performed in this work, which has also been used in order to perform the Laser Speckle Contrast Imaging (LSCI) technique subsequently explained.

The plane surface of the marquetry sample was observed by means of the CMOS camera discussed above and illuminated by a laser ($\lambda = 532 \text{ nm}$) of 250 mW power collimated with a lens and then expanded by a frosted glass. Through the above procedure, the speckle pattern was formed on the sample surface. The cold specklegram, i.e., the image acquired before the application of the thermal stress, as well as the images acquired during the cooling phase separated by a fix time interval, named *frame rate* (5 s), were digitized and stored into a PC as digital images. The analysis of the specklegrams enables the detection of potential displacements,

if searching for a matched point from one specklegram to another. Here it shall be stated that as it is almost impossible to find the matched point through a single pixel, thus an area of multiple pixels (i.e., 20×20 pixels) was used to perform the matching process. This area, named *subset*, had a unique light intensity (gray level) distribution inside the subset itself. It was assumed that this light intensity distribution did not change during deformation. The concept of the subset displacement on the specklegram before and after deformation is illustrated in Fig. 7. In practice, the speckles work as reference points which allow the matching of the content of two subsets.

Based on the above reported concept, the function implemented to match the subset from one image to another one, includes both the magnitude of the intensity value difference (Eq. 7), and the normalized cross-correlation (Eq. 8).

$$R(x, y, x^*, y^*) = \sum |F(x, y) - G^*(x^*, y^*)| \quad (7)$$

$$C(x, y, x^*, y^*) = \frac{\sum F(x, y) G^*(x^*, y^*)}{\sqrt{\sum F(x, y)^2 \sum G^*(x^*, y^*)^2}} \quad (8)$$

where, $F(x, y)$ and $G^*(x^*, y^*)$ represent the gray levels within the subset of the un-deformed and the deformed specklegrams, and (x, y) and (x^*, y^*) are the coordinates of a point on the subset before and after deformation, respectively. The symbol of the summation represents the sum of the values within the subset. The coordinate (x^*, y^*) after deformation relates to the coordinate (x, y) before deformation. Therefore, displacement components are obtained by searching the best set of the coordinates after deformation (x^*, y^*) which minimize $R(x, y, x^*, y^*)$ or maximize $C(x, y, x^*, y^*)$. In order to provide an adequate thermal stress on the marquetry sample, two Philips 250 W IR lamps were also used in this case. The heating phase lasted for 1 min and the lamps were posi-

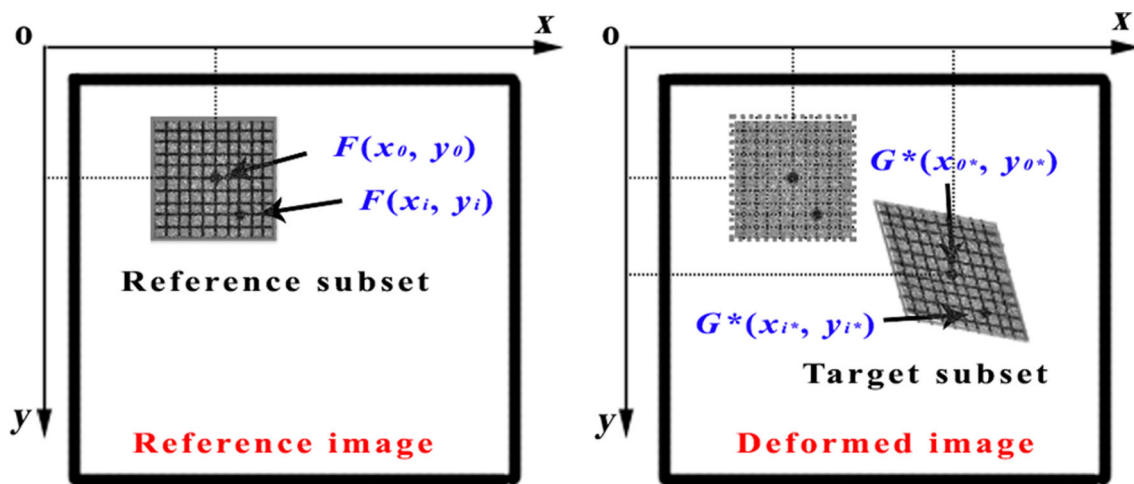


Fig. 7 The concept of the displacement of the subset between two different state

tioned at the same distance (0.810 m) with respect to the center of the marquetry sample. These technical data are also related to the LSCI technique.

2.2.5 Laser Speckle Contrast Imaging (LSCI) Technique

The experimental setup for LSCI is very simple, illustrated in Fig. 6. Laser light illuminates the object under investigation, which is imaged by a digital camera. The image is captured and processed by a script written ad hoc in Matlab[®] environment. Several parameters must be kept in mind; among these, the exposure time, the number of pixels over which the local contrast is computed, the scaling of the contrast map, and the choice of gray tones or colors for coding the contrast. The choice of the pixels' number over which the computation of the speckle contrast is calculated, it is also of great importance as too few pixels lead to the statistics being compromised and too many cause spatial resolution to be sacrificed. In the present study, it was found that a square of 5×5 pixels had a satisfactory compromise. Therefore, a square with sides of odd number of pixels was chosen so that the computed contrast was assigned to the central pixel. The speckle contrast K is quantified by the usual parameter of the ratio of the standard deviation to the mean ($\sigma / \langle I \rangle$) of the intensities recorded for each pixel in the square.

$$K = \frac{\sigma}{\langle I \rangle} \quad (9)$$

The pixel square is then moved along 1 pixel and the calculation repeated: this overlapping of the pixel squares results in a much smoother image than that obtained if using contiguous squares. This method is not time-consuming, the processing time is very low, and it does not require a high computational cost. Here it shall be stated that the overlapping of the squares does not lead to an increase in resolution, as resolution is only determined by the size of the used square: there is a trade-off between spatial resolution and reliable statistics.

LSCI technique allows the flexibility of choosing the local contrasting neighborhood N in either the spatial or the temporal domain or in combination of these two domains. This enables its spatiotemporal resolution to be tailored to the specific needs of individual applications. In practice, resolution can range from tens of micrometers in the spatial domain to sub-second scale resolution in the temporal domain, limited only by the frame rate of the imaging device.

The selection of the contrast in the spatial domain (s LSCI), is the oldest form of LSCI. This method provides the highest level of temporal resolution, while it compromises the spatial resolution. Instead, the selection of the contrast in the temporal domain (t LSCI), brings to a higher spatial resolution than this of s LSCI. Finally, spatiotemporal schemes use neighborhoods extending in both the spatial and temporal domains.

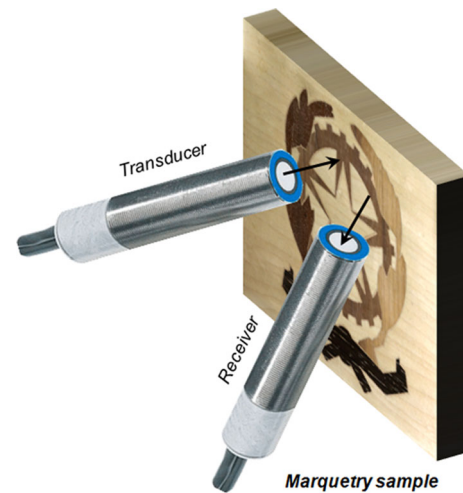


Fig. 8 UT experimental setup

In particular, temporal averaged spatial LSCI ($tavsg$ LSCI) first calculates local contrast in a spatial neighborhood and subsequently averages the calculated contrast value across a temporal neighborhood. The purpose of this method deals with the reveal of superficial anomalies linked to manufacturing process, which have to be correlated with the results coming from NIR technique [23–27].

2.3 Ultrasonic Testing (UT) Technique

The ultrasonic experimental setup used in this work is shown in Fig. 8. Considering the various wood types which constitute the decorative layer, the anisotropic nature of the wood, as well as the wood fibers disposition and the humidity content, the use of UT technique is very challenging. The system is composed of two sensors: the transducer (T) and the receiver (R).

In the present study, the V-Meter MK III ultrasonic system has been used. It consists of a pair of transducers and a pulse-receiver unit, while the indirect surface transmission testing configuration was selected [28]. The aim of this testing was to measure the travel time of the ultrasonic wave into the wooden panel bulk and perform comparative evaluations after applying the same measurement both on the sound and defective wooden panel. Through this experimental setup, the transmitting and receiving elements have been placed on the surface of the wooden panel at the end points of a line that will be in-depth illustrated into Sect. 3. The measurements have been carried out at the higher frequency, this of 2 MHz, while transducers were coupled to the surface thanks to a suitable elastic couplant (i.e., plasticine). In order to ensure the reliability of results, during each individual line inspection, the coupled pressure was steadily increased until the measured transmission time was reaching a constant value; therefore, the pressure applied during each individual inspec-

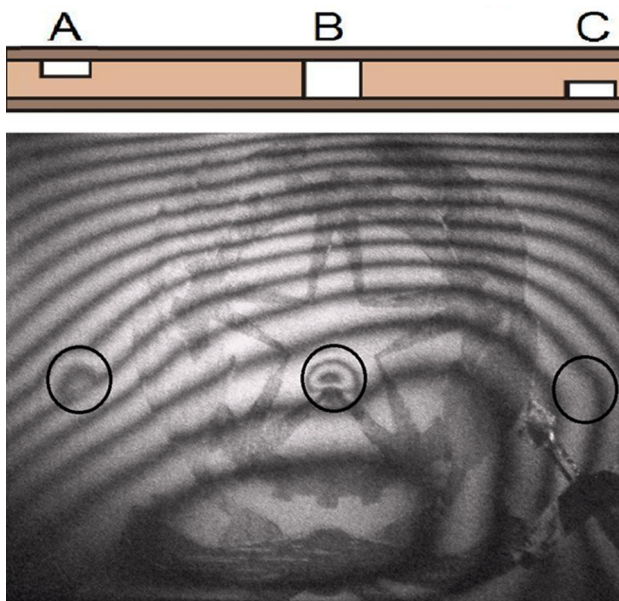


Fig. 9 Interferogram of the marquetry sample acquired through the DE method

tion can be considered as an independent parameter that is not influencing the reliability of measurement.

3 Results and Discussion

As can be seen from the DE interferometric result presented in Fig. 9, the fabricated flaws (A–C) positioned inside the three layers (1–3—see Fig. 1) caused local deformations due to the different temperature gradients occurred in the various sections of the marquetry sample. To obtain such hologram, the experimental setup remained stable within a fraction of a micrometer; in fact the experiment was performed on a vibration-isolated heavy table.

Each flaw manifests itself through the local change of the interference fringes, from a regular pattern to a round-shape pattern above the voids. The air bubbles occurring inside the A–C flaws conduct the heat transfer in a more difficult manner with respect to the areas in which a good contact between the layers is exhibited. Nevertheless, the deviation of the fringes pattern due to the presence of flaw C produced a very weak contrast, which can be attributed to the continuous and broader heating source used (heat supply was performed from the decorative side of the panel). In fact, if the heating source is either continuous (i.e., with a duration much longer than the thermal propagation time through the layer thickness) or broaden than the delaminated area, or both, a radial strain field will be established with little buckling effect unless the layer is initially convex [29,30]. However, this type of heating source (i.e., lamps or ceramic infrared radiation sources) has been extensively used into the cultural heritage

field, and linked to HI technique for the detection of similar defects [31,32]. As anticipated in Sect. 2.2.1, same result can possibly be obtained by attaching the sample to a source of vibration. In this case, the thin layers of material above defects A and B would be oscillating with higher amplitude compared to other surface points, which (while observed in the same setup) may lead to same image detected. Unfortunately, the authors do not have this type of component at the moment in which the paper is written, although they think to explore this interesting idea as future perspective of the present research work.

Moreover, it is very interesting to notice that no information can be retrieved about the position of the superficial flaw D (putty). The above representative result indicates that the thermal parameters play an important role both in the interferometric measurements and the thermographic measurements (considering that results interpretation in this case is also based on the study of heat diffusion). Thus, this issue was studied in-depth starting from a research bibliography [33,34] of the most important technical characteristics of the materials used during the manufacturing of the sample (Fig. 10), and arriving to a numerical simulation realized in Comsol® Multiphysics.

For the Comsol Heat Transfer Module in order to simulate the heat transfer process, the following steps were implemented: (a) *Geometric modelling* According to the object's shape and its volume, a 3D model was established, (b) definition of *physics settings*. Physics menu contains two setting options, which are the sub-domain settings and the boundary settings. *Sub-domain settings* is for setting each domain's material property, initial conditions, etc., and the *Boundary settings* is for setting the boundary conditions in two aspects. During this step, initially the boundary conditions on the interface of the different materials were adjusted, followed by the adjustment of the boundary conditions on the interface between the modelled panel and the environment. The last step is (c) *Solving process*, where the proper solver was selected, linked to the problem to be analyzed, and not the default setting.

Of prime importance for successfully simulating the actual inspection scenario, is the accurate creation of the physical model (geometric modelling). In the present study, this step was not easy to be addressed considering the irregular shape of the coat of arms. Thus for realizing a geometric model as more realistic as possible, the authors followed the main steps reported on flow chart of Fig. 11.

By assigning the proper technical characteristics, presented in Fig. 10, into each area, the respective numerical solutions were obtained and illustrated in Fig. 12. In particular, the temperature evolutions through the sample were analyzed by considering the main vertical sections inherent to the flaws A (Fig. 12a, b), B (Fig. 12c, d), and D (Fig. 12e, f). However, referring e.g. to the sequence of points of Fig.

TECHNICAL CHARACTERISTICS OF THE MATERIALS USED												
MATERIALS	DENSITY lowest/medium/highest [Kg/m ³]	Lowest DENSITY [g/cm ³]	Medium DENSITY [g/cm ³]	Highest DENSITY [g/cm ³]	Thermal CONDUCTIVITY [W/mK]	Lowest KOLMANN' conductivity [Kcal/mh°C]	Medium KOLMANN' conductivity [Kcal/mh°C]	Highest KOLMANN' conductivity [Kcal/mh°C]	Lowest KOLMANN' conductivity [W/mK]	Medium KOLMANN' conductivity [W/mK]	Highest KOLMANN' conductivity [W/mK]	SPECIFIC HEAT at constant pressure [J/KgK]
Maple	530-660-790	0,53	0,66	0,79	0,18	0,11104	0,13288	0,15472	0,095477214	0,114256234	0,133035254	1159,74
Mahogany	600/620/1010	0,06	0,062	0,101	0,0278	0,03208	0,032416	0,038968	0,027583835	0,027872743	0,033506449	1159,74
Walnut (whitish part)	600/700/900	0,06	0,07	0,09	0,029	0,03208	0,03376	0,03712	0,027583835	0,029028375	0,031917455	1159,74
Wengè	675/840/1005	0,067	0,084	0,1	0,031	0,033256	0,036112	0,0388	0,028595013	0,031050731	0,033361995	1159,74
M.D.F	400/530/630	0,04	0,053	0,063	0,0265	0,02872	0,030904	0,032584	0,024694755	0,026572657	0,028017197	1159,74
Putty	1650				0,1866							1380
Walnut (core part)	900				0,0319							1159,74

Fig. 10 Technical characteristics of the materials used during the manufacturing of the sample

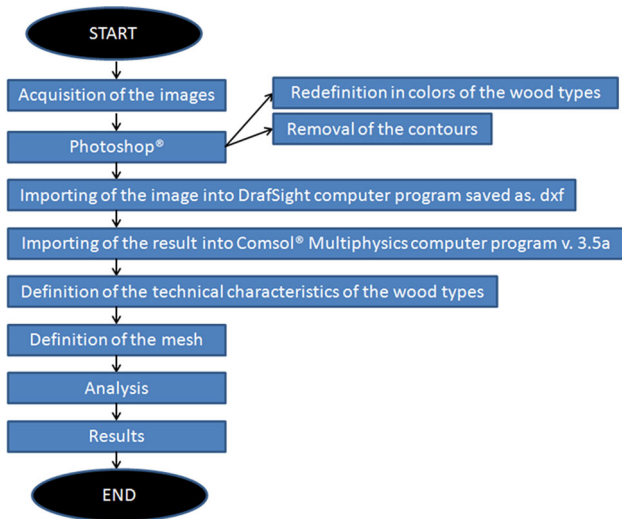


Fig. 11 Flow chart showing the main steps implemented in order to perform the numerical simulation

12b, lying on the vertical of the defect A passing through its centroid, the temperature trends for time intervals (from 0 to 120 s, equi-spaced of 5 s), are presented on the right of the graph. Indeed, it is the time bar expressed in seconds [35].

In the following, the choice to express along the abscissa the specimen thickness by means of the Arc-length factor is related to the numerical solution of the problem. From the flow chart of Fig. 11, it is possible to notice that the problem analysis occurs as a result of the mesh model. In the finite element method (FEM), the solution is calculated in the nodes that discretize the structure. In particular, the nodes discretize the geometry, in local coordinates, as can be seen in Fig. 13a. After the analysis, the information is known

on the node. In that respect, it is necessary to reconstruct the final information used by the user on the real geometry, but in global coordinates. In Fig. 13b, both the reconstruction phase and the passage of coordinates are shown.

In fact, assuming that the arc-length factor is equal to Eq. (10):

$$S \equiv \int_{\gamma} |dl|, \tag{10}$$

where S is the curvilinear integral in γ , then dl is:

$$dl = dx\hat{x} + dy\hat{y} \tag{11}$$

and, developing $|dl|$ of Eq. (11) in Eq. (12), it is possible to obtain:

$$ds = |dl| = \sqrt{dx^2 + dy^2} \tag{12}$$

In addition, dividing by dx both members:

$$ds = \sqrt{\frac{dx^2}{dy^2} + 1} dx \tag{13}$$

then, the generic curvilinear integral is calculated in Eq. (14).

$$S \equiv \int_{\gamma} |dl| = \int_{\gamma} ds = \int_a^b \sqrt{\frac{dx^2}{dy^2} + 1} dx \tag{14}$$

in which, a and b represent the extremes of the curve conveniently substituted.

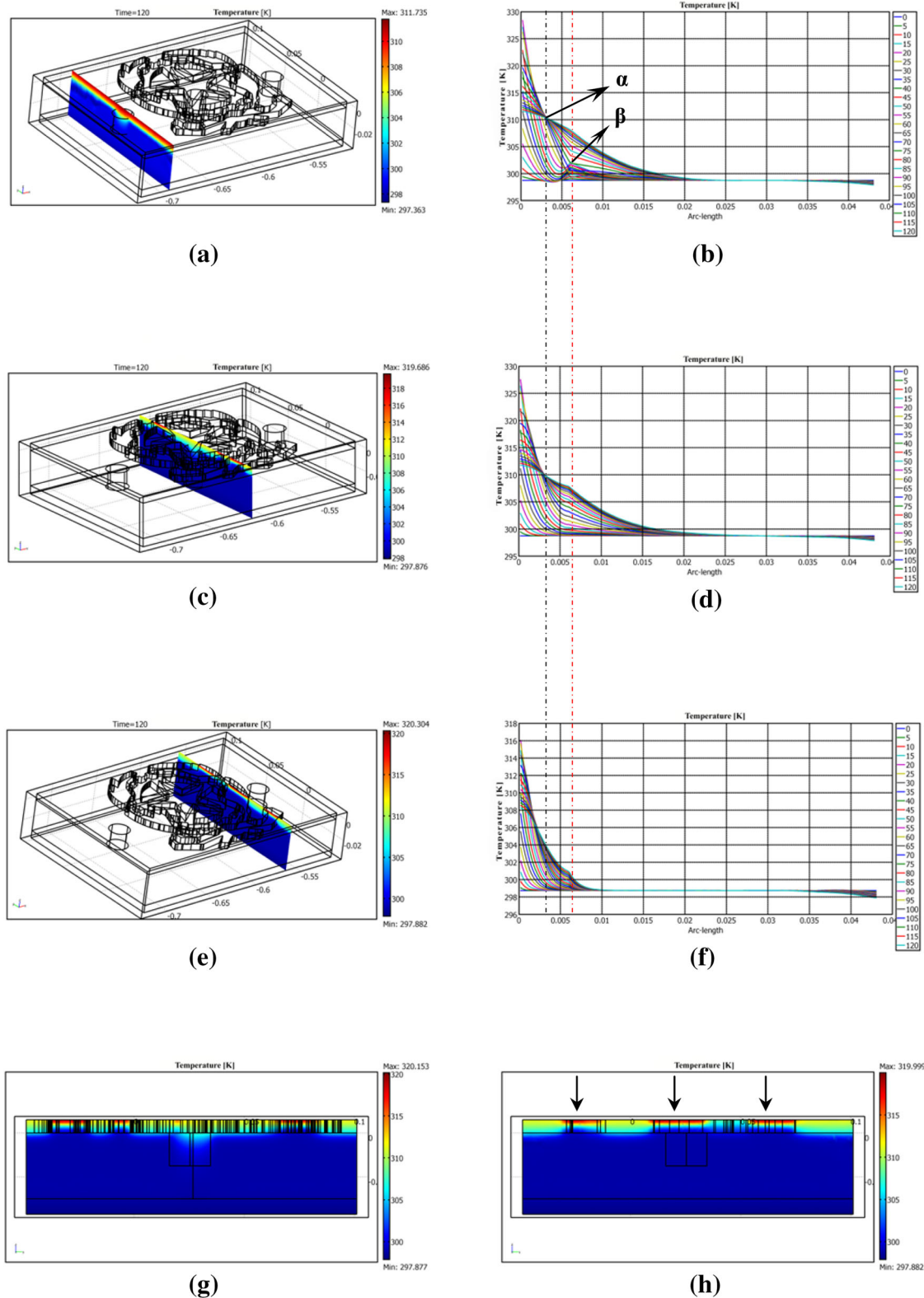


Fig. 12 Numerical simulations: **a** 3D heat diffusion passing through the A flaw at the end of the cooling stage (120 s), **b** entire evolution of temperature inherent to the cross-section shown in (a), **c** 3D heat diffusion passing through the B flaw at the end of the cooling stage (120 s), **d** entire evolution of temperature inherent to the cross-section shown

in (c), **e** 3D heat diffusion passing through the D flaw at the end of the cooling stage (120 s), **f** entire evolution of temperature inherent to the cross-section shown in (e), **g** 2D heat diffusion passing through the B flaw, and **h** 2D heat diffusion passing through the D flaw (Color figure online)

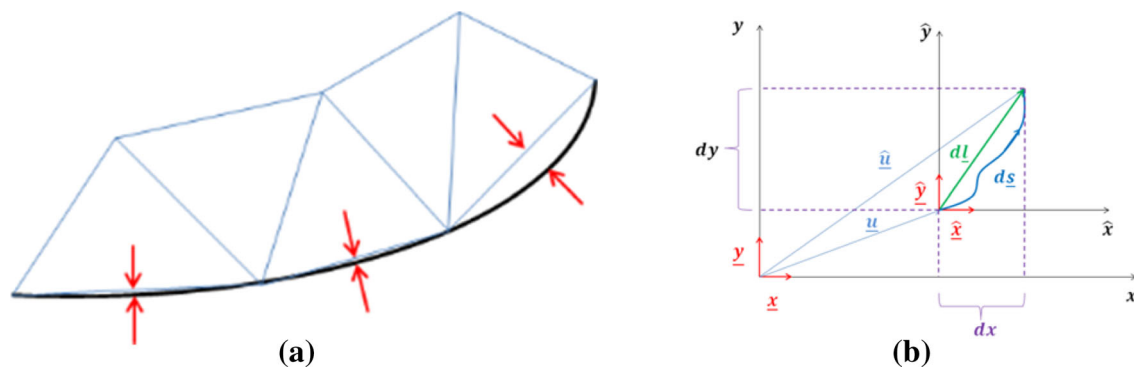


Fig. 13 Arc-length explanation: **a** discretization of the structure via the mesh. The *arrows* show the existing approximation between the mesh and a part of the real profile in a situation of considerable magnification, and **b** graphical reconstruction of the mathematical concept of arc-length

Two characteristic points (α and β) on the plots of Fig. 12, signalled by two dotted lines, are of interest. The first one appears for the flaws A and B just before 0.005 Arc-length along the horizontal axis, and at ≈ 310 K along the vertical axis. Instead, the corresponding characteristic point for flaw D appears in a previous moment and at a lower temperature than that signalled by the dark dotted line.

The α point is of interest because, up to the maximum wall temperature, this value remains stable at ≈ 310 K; the β point is important because it indicates the maximum phase shift, i.e., when the wall temperature is maximum, the value of the temperature in β is minimum. By varying the temperature of the wall, the β point translate rigidly along the direction indicated by the dashed red line (Fig. 12b, d, f). Although the representation shown in Fig. 12b, d, f may appear at a first glance uncertain due to the line-color matching, it is shown as such because the time interval set at 5 s exalts the peculiarities of the intersection of the 25 temperature evolutions on the two characteristic points (α and β) before enounced, which could remain vague at an interval of, e.g., 15 s.

The explanation of this phenomenon is linked to the presence of the voids along the external and central sections, as well as it is connected to the difference in the thermal inertia between the putty insert and the different type of woods.

In particular, the discontinuity of the third type marked by a red line (β) shows a phase displacement of the temperature between each position indicated along the Arc-length direction with respect to the thermal source. This is happening at a different temperature with respect to the other two discontinuities, because it is strictly linked to the depth of each flaw. The 2D views of Fig. 12c and e are reported on Fig. 12g and h, respectively. It is interesting to notice that, at the end of the cooling stage, flaw B maintains a higher temperature along the z axis with respect to flaw D. The latter flaw, at this time (120 s), has effectively released the trapped heat due to its lower thickness. This phenomenon did not appeared on the three parts consisting of both the wenge and the walnut (whitish part) types of wood. Readers can com-

pare the positions indicated by the three arrows in Fig. 12h with the section marked by a dotted line in Fig. 1. Indeed, inside these areas, the temperatures are higher in reference to the surrounding part made by maple wood. This result is validated by considering the technical characteristics of the materials used and reported for reference in Fig. 10.

In synthesis, the plots reported in Fig. 12 show the temperature field into a fixed temporal instant that is linked to a specific section of the sample. By assuming that the model reflects perfectly the reality, by cutting the sample following the assigned directions and measuring at 120 s the temperature field, it is possible to obtain the results proposed in Fig. 12g, h. Along with the gain of knowledge for the interaction of the internal flaws to a given heat energy supply, supplementary information regarding the rate of the provided heating by the source is also useful when inspecting, in a non-destructive manner the samples and when the efficient conductive propagation of the thermal waves to the whole volume of the flaws has to be ensured. The emitted heat flux was determined starting from the research work published in [36]. Particular attention was given to the influence of the view factor of the lamps when referred to the shape of the analyzed sample. For this reason, a Matlab[®] script written *ad hoc* was realized. The Matlab[®] script took into account both the relative intensity, the spectral distributions of the Siccatherm[®] lamps (Fig. 14a–d) and the corrective coefficient linked to the degradation factors inherent to the lamps, such as the ageing of the lightbulb and the loss or gain of irradiance during the time of exposure [37,38].

The main information about the IRT experimental setup are reported in Fig. 5. The temperature deviations observed during the thermographic analysis are in good agreement with the numerical simulations shown in Fig. 12. Although the graphs indicate temperature deviations equal to ≈ 30 K, it is important to remember that the object analyzed is: (a) constituted by pieces of woods coming from the furniture sector, and (b) it is without a painted layers made by pigments. Before to be analyzed at infrared, the pieces of wood

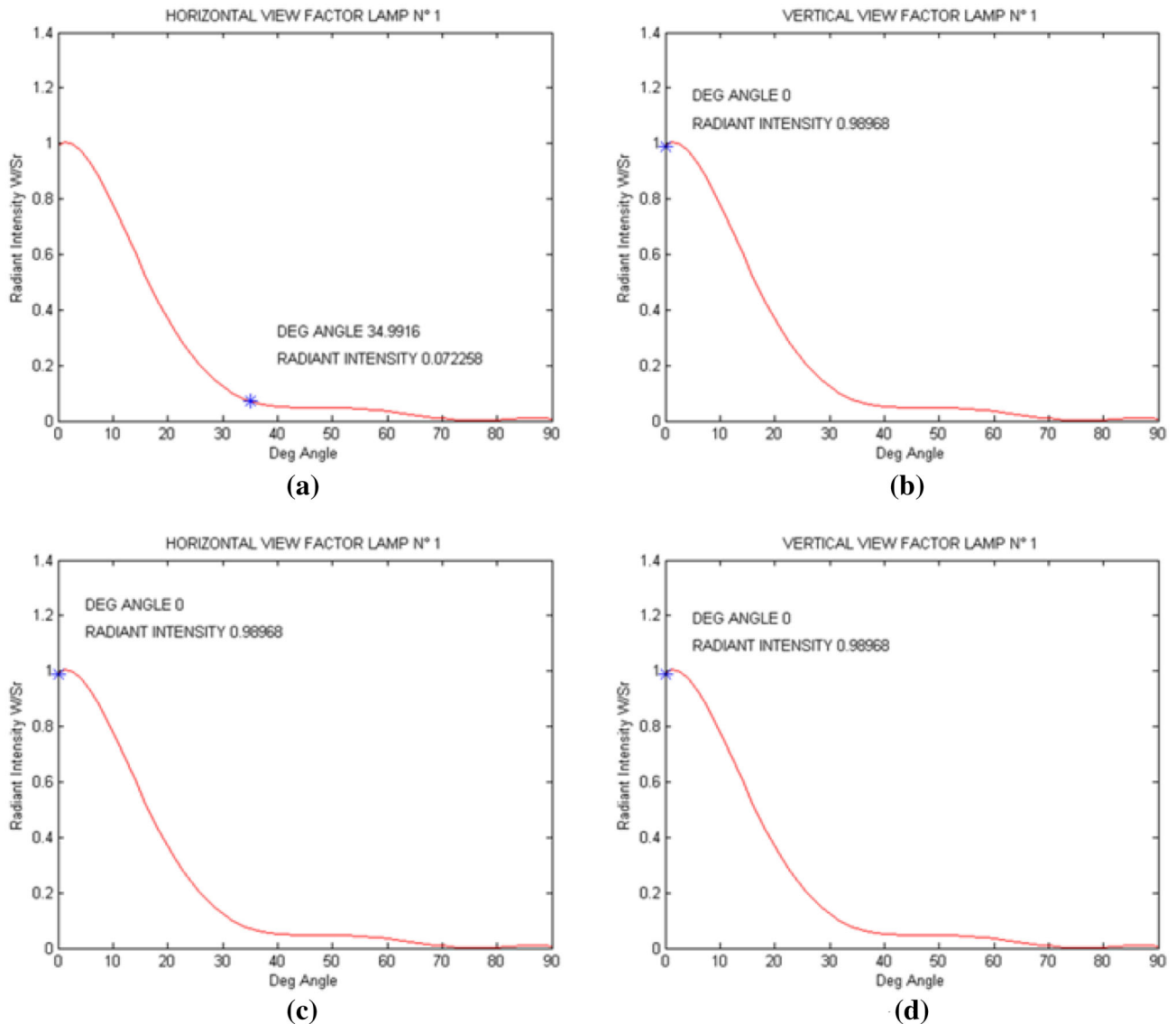


Fig. 14 **a** Horizontal and **b** vertical view factors inherent to one lamp positioned in reflection mode; **c** horizontal and **d** vertical view factors inherent to the one and only lamp positioned in transmission mode

undergone a thermal treatment. Indeed, the target core temperature of 55 °C was kept in a climatic chamber for at least one hour to ensure successful for the annihilation of possible insects [39]. The ΔT reached in the experiment shown herein is below this level. The same maximum temperature (around 50–60 °C) is reached during the application of the hot glue (also known as animal glue) usually applied in this type of objects by the restorers [40]. Therefore, the type of thermal stress used herein is completely nondestructive, taking into account what happens during the manufacturing of these type of objects.

In particular, the reader can notice two halogen lamps, with the caps highlighted by means of a red color. The lamps have been positioned at 35° angle with reference to an ideal

perpendicular axis (that is highlighted by means of a red dotted line in the same figure) passing through the center of the defected sample. The heating and the cooling periods were fixed at 1 min and at 150 s, respectively. The thermograms were acquired at every second; in practice, two hundred and eleven thermograms were collected, also considering the cold image. The infrared camera was initially installed in reflection mode at 0.88 m distance (\overline{BC} distance in Fig. 5), while during the data acquisition in transmission mode, one of the two lamps was moved from the front to the rear side. The geometrical information played an important role in order to obtain the plots reported in Fig. 14, while the time of thermal exposure has been selected by following the guidance of the numerical model schematized in Fig. 12. The cooling

phase, strictly linked to conduction phenomena, as well as to the heating phase, has been established by considering a .avi video realized in Comsol® Multiphysics which represents the spatial-temporal temperature field.

In the transmission’s case modality, the heating time was increased up to 80 s, taking into account the modification carried out to the experimental setup. Moreover, a timer was used in order to monitor the switching on and off of the lamps, as well as the total time of the IRT data acquisition. Some output values are reported in Fig. 5, while the applied heat flux, was equal to 1018.2 W/m² in the first case and 7353.1 W/m² in the second case.

The Stefan–Boltzmann equation calculates the net energy radiated by the heater. It does not calculate how much of the radiated from the source energy actually hits a body. Nevertheless, there is a geometric relationship between the size of the heater and the body, the distance between them and the reciprocal positions of the surfaces. All together, these factors determine how much of the radiated energy the body intercepts. This relationship is called the view factor.

In the following is explained why the view factor between a surface *i* and a surface *j* is independent by the emissivity value of the body. From a mathematical point-of-view, it can be determined as in Eq. (15):

$$F_{i \rightarrow j} = \frac{q_{i \rightarrow j}}{q_i} \tag{15}$$

where, $q_{i \rightarrow j}$ is the flow of radiant energy emitted from the surface *i* which hit the surface *j*. It can be expressed as in Eq. (16), where the $I_{i,\theta}$ factor is introduced. It is the intensity of the directional emission, which is constant for θ . This assumption is valid for spherical broadcastings. Therefore, it can be put outside of the integral as in the following.

$$q_{i \rightarrow j} = I_i \cdot \int_{A_j} \int_{A_i} \frac{\cos \vartheta_j \cdot \cos \vartheta_i}{R^2} \cdot dA_i \cdot dA_j \tag{16}$$

Concerning q_i , with the assumption of the constant emission for θ , Eq. (17) can be obtained.

$$q_i = A_i I_i \int_{\Omega} d\Omega = A_i \pi I_i \tag{17}$$

with, Ω the solid angle is represented. Therefore, because the I_i factor is simplified into the ratio $F_{i \rightarrow j}$, which was developed for the entire area of integration, Eq. (18) can be found.

$$F_{i \rightarrow j} = \frac{1}{\pi A_i} \int_{A_j} \int_{A_i} \frac{\cos \vartheta_j \cdot \cos \vartheta_i}{R^2} \cdot dA_i \cdot dA_j \tag{18}$$

For a sake of clarity, in Fig. 15 the schematization which corresponds to the determining of the view factor for a non-monochromatic radiation outgoing from an emitting surface

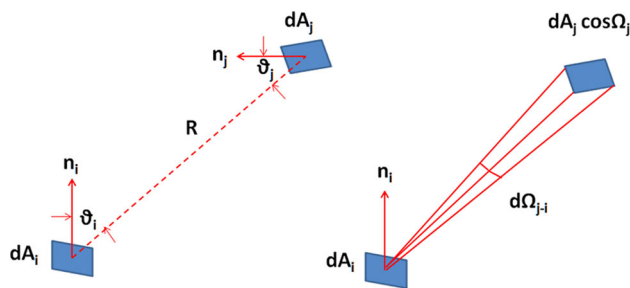


Fig. 15 View factor linked to the exchange of radiant heat between two surfaces

(i.e., the lamp) and entering into a receiving surface (i.e., the marquetry sample) is shown.

Starting from Eq. (18), the view factor can be determined graphically in Matlab® environment. The innovation in this work is that for the determination of the view factor, the abacuses were not used. In particular, it was separately analyzed on the horizontal (Fig. 14a) and the vertical (Fig. 14b) views, considering that non-parallel planes constitute the experimental setup.

To sum up, the view factors establish the percentage of the radiant energy leaving the lamps that is intercepted by the marquetry sample. However, in the present case, it is not convenient to separate the view factors from the radiant intensity values (indeed, the latter is the pivotal point of the discussion, which is, in quantitative terms, enounced in Fig. 14a–d) in order to obtain the estimation of the applied thermal fluxes on the marquetry sample. In fact, the goal was to determine the radiant intensity on the receiver surface (i.e., the decorated surface of the marquetry sample).

Bearing in mind the symmetrical positions of the lamps with respect to the sample, Fig. 14a, b only show two graphs linked to one lamp, since the other two are redundant. Indeed, Fig. 14c, d clarify what happens for the setup in transmission mode (Fig. 5). The validation of the experimental method is proven looking at the thermographic results of Fig. 16.

In particular, the experimental results were found to be in a good agreement with the numerical simulations, as flaw B was efficiently detected having the strongest contrast among the flaws. The efficient detection of flaw B was also confirmed through the results derived by the application of HI technique (Fig. 9). Here it shall be noticed that the numerical calculations predicted the retention of a high temperature at the end of the cooling phase (Fig. 12g), which was also confirmed by the different PCT results (Fig. 16a–c) leading to the best visualization of this flaw. The above experimental and numerical results can be linked to the fact that this flaw had the greatest thickness among the three voids (Fig. 1). Moreover, the quasi-unperceivable lost of the signal in the detection of flaw A among the results in reflection (Fig. 16a, b) and transmission (Fig. 16c) mode, guarantees the success

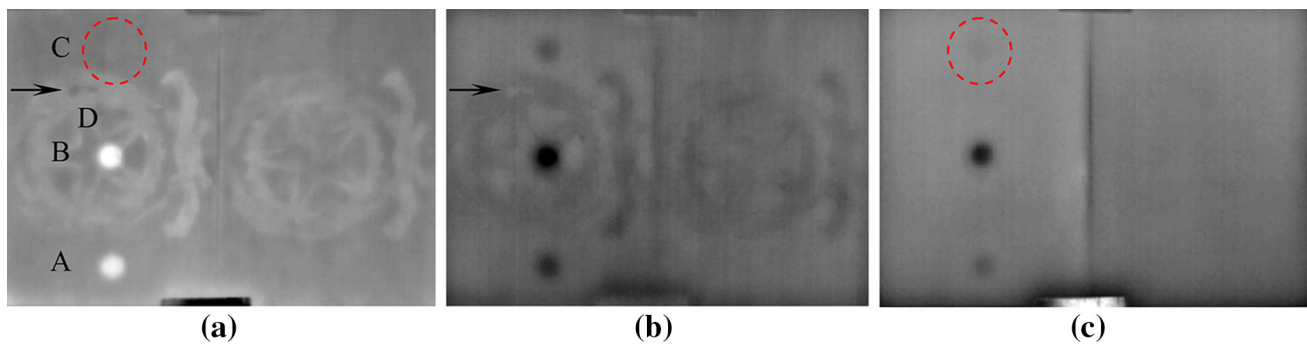


Fig. 16 Comparative thermographic results from the defective (*left side*) and defects-free (*right side*) samples by using a FLIR ThermoCAM S65 HS camera. Reflection mode: **a** PCT-EOF₃, **b** PCT-EOF₅. Transmission mode: **c** PCT-EOF₂

of the experimental results reported in Fig. 16, bearing in mind the very close position of this flaw with respect to the front side (Fig. 1). Furthermore, flaw C was also detected in both modes even that its produced contrast was very slight. It is the deepest flaw, and it is surrounded by a dotted circle in Fig. 16a, c. Finally, the PCT technique, in the reflection mode, was also able to detect the shape (see the arrows in Fig. 16a, b) of the very thin layer of putty (flaw D), as well as to map by a different intensity color the area, with respect to the symmetrical region (Fig. 1).

Another set of raw thermographic data were subsequently recorded by a FLIR ThermoCAM SC640 camera, and analyzed by TSR technique. Through the calculation of the first time and second time derivative images, the defect visibility was assessed investigating the temporal variations of the cooling rate (1st derivative) and the temporal variations of the acceleration (or deceleration) of this cooling rate (2nd derivative). The derivative images were acquired after reconstructing the raw temperature data to the synthetic one, through a 4th degree polynomial fitting function. Representative 1st time derivative and 2nd time derivative results after treating the whole sequence (heating up and cooling down phases), are illustrated in Fig. 17a and b, respectively. In each individual TSR result, the top half area corresponds to the sound panel while the bottom half to the defective panel.

In general, the derivative analysis enhanced both the flaw visibility and sensitivity regardless their location. An additional factor leading to the above stated enhancement could be the fact that the current infrared camera had a double image resolution with respect to the device used for the PCT analysis (see Table 1). The application of TSR along with data recording from a high resolution thermal camera provided, in addition, the detection of two interesting features. The first one is a radial image artifact which appears around the A and B flaws both in the 1st (Fig. 17a) and in the 2nd time (Fig. 17b) derivative images, while the second one seems apparently to be linked to the detection of the wooden texture of the wooden maple (Fig. 1), arranged along a horizontal

direction. Finally, the detection of the flaw D, signaled by an arrow, is confirmed also in this case, while the flaw C, surrounded by a dotted circle, is weakly revealed if compared to the PCT-EOF₅ result presented in Fig. 16b.

The detection of the alignment of the wooden texture of the upper layer of the marquetry sample was confirmed by using the LSCI technique. The optical results are shown in Fig. 18. In this analysis, the authors started to explore the superficial condition of a part of the coat of arms of the Italian Republic by enhancing the speckle contrast with respect to the probability density function (PDF), and taking into account a defect-free area, named background area in the graph of Fig. 18a, inherent to the wooden maple. The result shown in Fig. 18b details some small gaps like needles (see the white parts) in the wooden walnut (core part). In order to explore more in-depth this part of the sample, the spatial contrast has been correlated to the temporal contrast by considering two different speckle patterns, i.e., by knowing the frame rate ($5\text{ s} \times 4$ intervals). Also during the speckle measurements, the images—called, specklegrams—were acquired in reflection mode. In addition, the time of the heating phase (60 s) adopted during the thermographic acquisitions performed at the University of L'Aquila (Italy), as well as the type/number/and disposition of the lamps, have been confirmed in order to obtain the results subsequently proposed (Fig. 18).

It is possible to notice how the graph changes from the PDF spatial contrast (Fig. 18c) to the combined PDF of the spatial and temporal contrasts (Fig. 18d); in particular, the noise which appears during the in-plane speckle diffusion in the second part of the graph, it is smoothed in the course of time. The result reported in Fig. 18e, clearly reveal the maple wooden texture which acts along the horizontal direction. Thanks to a superimposition process, also the DIC result of the B flaw is reported in the same figure. It is shown in the *magnitude* configuration that is the more pertinent for the present case [41]. The more important displacements are located above the B flaw, instead the DIC technique was not able to reveal the presence of the other sub-superficial

Fig. 17 Comparative thermographic results from the defective (*lower part*) and defects-free (*upper part*) samples by using a FLIR ThermoCAM SC640 camera. Reflection mode: **a** 1st time derivative image at $t = 0.533$ s, and **b** 2nd time derivative image at $t = 0.533$ s from a 4th degree polynomial fitting function

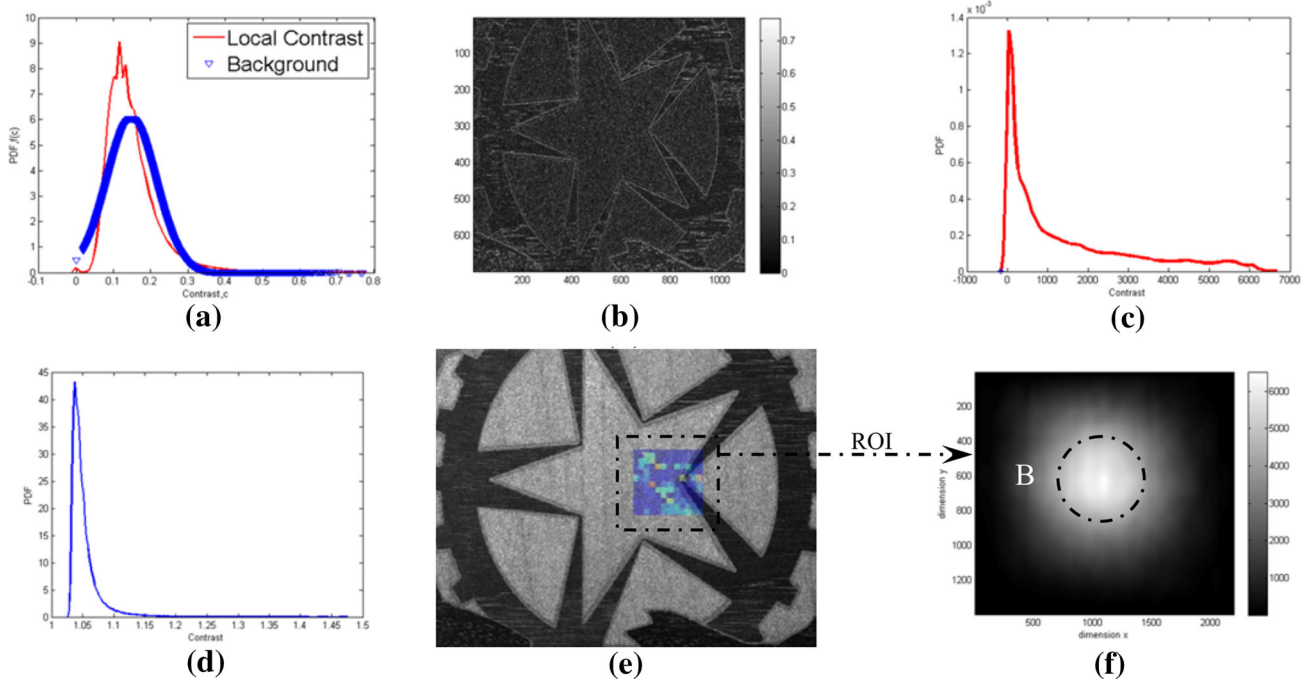
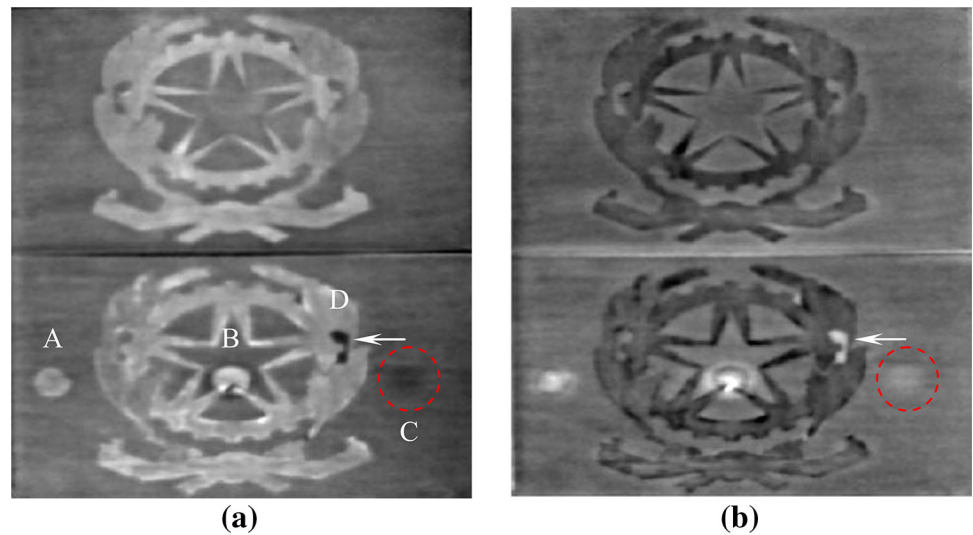


Fig. 18 **a** PDF (local and background) of spatial contrast image, **b** speckle contrast result, **c** spatial contrast PDF graph inherent to two non-consecutive speckle patterns, **d** PDF of the combined spatial and temporal contrasts, **e** DIC and LSCI results by processing two non-

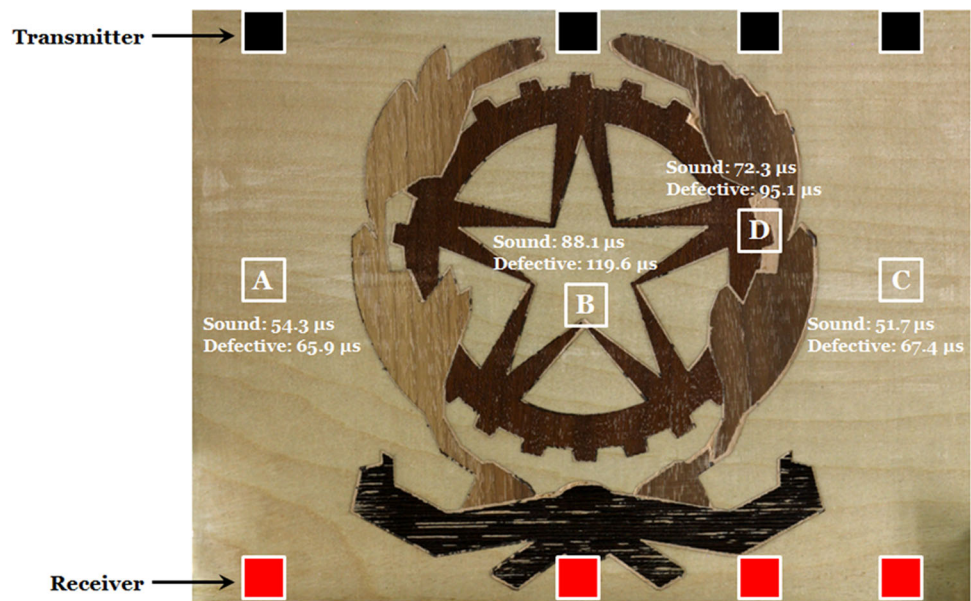
consecutive speckle patterns, and **f** LSCI result inherent to the B flaw thanks to a ROI, obtained by processing five consecutive speckle patterns

flaws with respect to the defect-free area and/or the defect-free sample. In order to assess the correlation, obviously, the two speckle patterns already used during the LSCI image processing were selected. Intensifying the speckle patterns acquired along the cooling phase, that were recorded between the images considered in the case illustrated herein, as well as by reducing for computation reasons the inspected area into the region of interest (ROI) signaled in Fig. 18e, the result shown in Fig. 18f was obtained. In particular, the B flaw was

detected (see the dotted circle) by processing five consecutive speckle patterns, and without losing, in the same time, the visualization of the horizontal alignment of the texture of the wooden maple.

The two wooden panels were further investigated through the aid of UT in order to confirm the surface and inserted flaws. As can be seen from the measured travel times summarized in Fig. 19, deviations were observed in this quantity for the same path of inspection but on a different panel. In

Fig. 19 Lines of inspection of the wooden surfaces showing the position of the transmit-receive transducers with respect to the position of the defects tested. In each path of inspection, the time taken for the ultrasonic wave to travel inside the inspected lines both on the sound and the defective wooden panel are also presented



practice, during the UT measurements, the authors worked through a comparison between the defective and the defect-free samples.

For instance, the travel time in line A was measured to be 54.3 μs on the sound panel while from the same inspection line at the defective panel, the travel time was measured to be 65.9 μs . The above deviation is indicating the greater sound attenuation degree presented in the latter inspection, which can be attributed to the presence of the flaw A. Similar results were also retrieved for the case of the flaw C, while increased travel times were also detected in the case of B and D flaws. Nevertheless, an increased travel time was observed from the inspection at line B, both on the sound (88.1 μs) and defective panel (119.6 μs). The increased time measured from the sound panel inspection can be possibly attributed to the different decorative interfaces into which sound has to propagate, producing in such a manner a regime of higher attenuation degree. On the other hand, the energy of the sound in the defective panel, along with the above-discussed parameter, is further attenuated due to the presence of the largest flaw B.

The latter flaw appeared in a clearest way by using the NIRT technique (Fig. 20c–j). In particular, by referring to the visible image acquired in reflection mode (Fig. 20a), the readers can see how the detection of the sub-superficial voids improve from 360 (Fig. 20b) to 1000 nm (Fig. 20h).

In addition, their detection enhances by using LED lamps working from 850 (Fig. 20i) to 940 nm (Fig. 20j). The reflection of the stand is missed using these LED lamps, while it is evident by working at the same wavelengths with the filters mounted on the camera (Fig. 20f, g). Some minor flaws (marked by yellow arrows) were detected at higher wavelengths (Fig. 20i, j). Through a comparison with the other

two flaws, the central B flaw was confirmed to be very shallow and thick. The UV result at 360 nm acquired in reflection mode (Fig. 20k) enhanced the wood grain, and also revealed a superficial flaw probably due to organic material. Observing the NIRR result (Fig. 20l), the state of conservation of the defective sample appears deteriorated if compared to the defect-free sample (see the internal area of the dotted rectangle in Fig. 20l). The putty insert (D flaw) was not detected by using NIRR nor NIRT techniques. Finally, the internal contour of the star of the defective sample appears dark by using the NIRR technique (Fig. 20l). This anomaly is surely linked to the laser cutting adopted for the marquetry production (Fig. 2s), although it does not appear in the defect-free sample. Therefore, the carbon-based material produced after the laser cutting acts as a revelator of the quality of the manufacture process, when inspected into the near-infrared region.

4 Conclusions

The joint use of NDT techniques is nowadays highly desirable for the inspection of artistic objects having a great importance, not only in term of cost. In this work, the authors focused their attention on two marquetry samples realized thanks to the laser cutting technique. Sometimes, it was possible to inspect only the defective sample in order to obtain a clear map of the surface and internal flaws, contrary to the UT inspection, where study in term of comparison between the defective and the defect-free samples was considered an interesting idea in order to obtain the same purpose.

Each technique adds details about the state of conservation of the sample under inspection, which are of interest for the

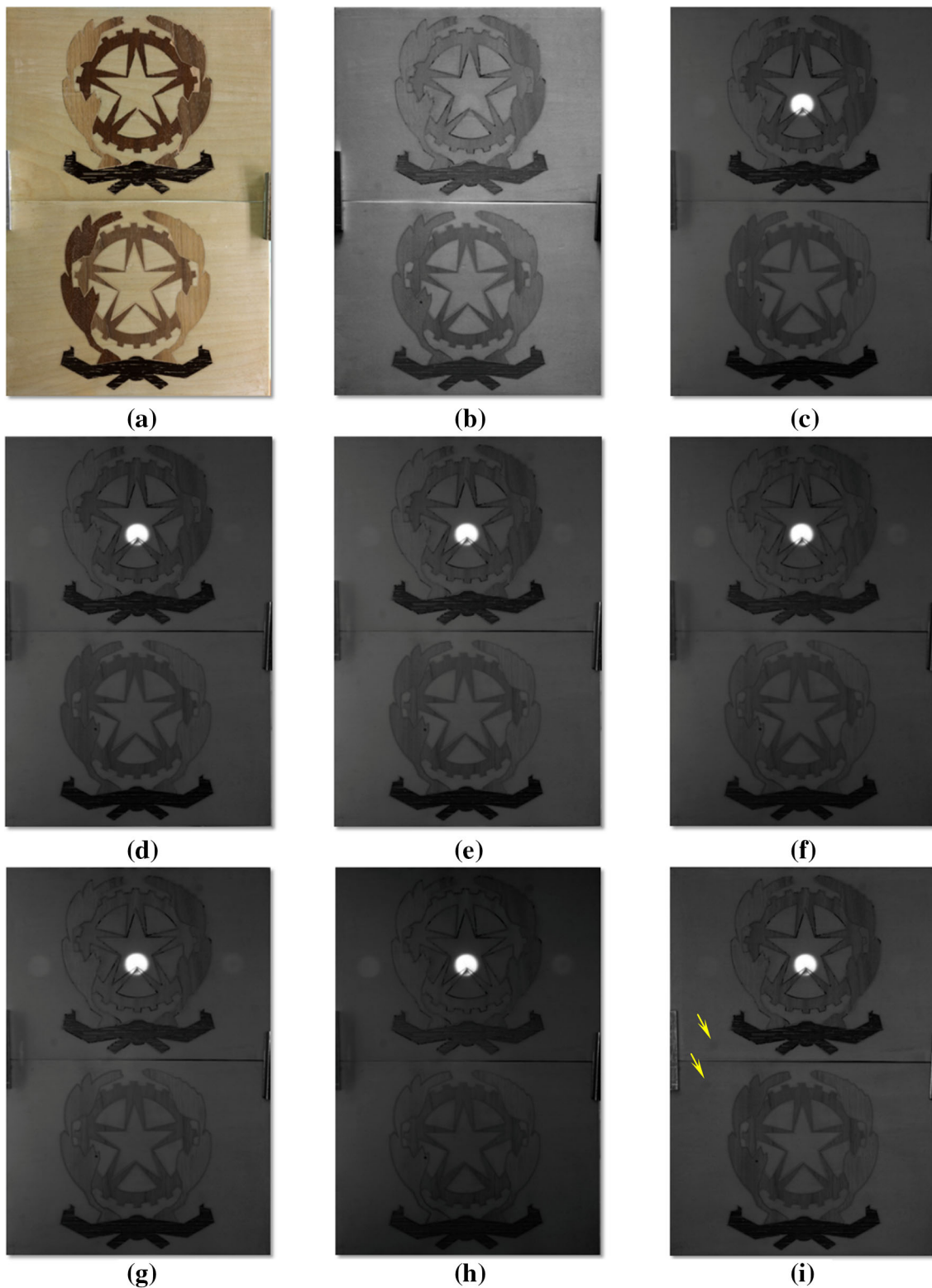


Fig. 20 Comparative imaging results of the defects-free Marquetry sample (*lower part*) and defective Marquetry sample (*upper part*) with **a** visible image, and with UV/NIRT results acquired at: **b** LED 360 nm,

c 680 nm, **d** 715 nm, **e** 760 nm, **f** 850 nm, **g** 950 nm, **h** 1000 nm, **i** LED 850 nm, **j** LED 940 nm. UV/NIRR results acquired at: **k** LED 360 nm, and **l** 680 nm (Color figure online)

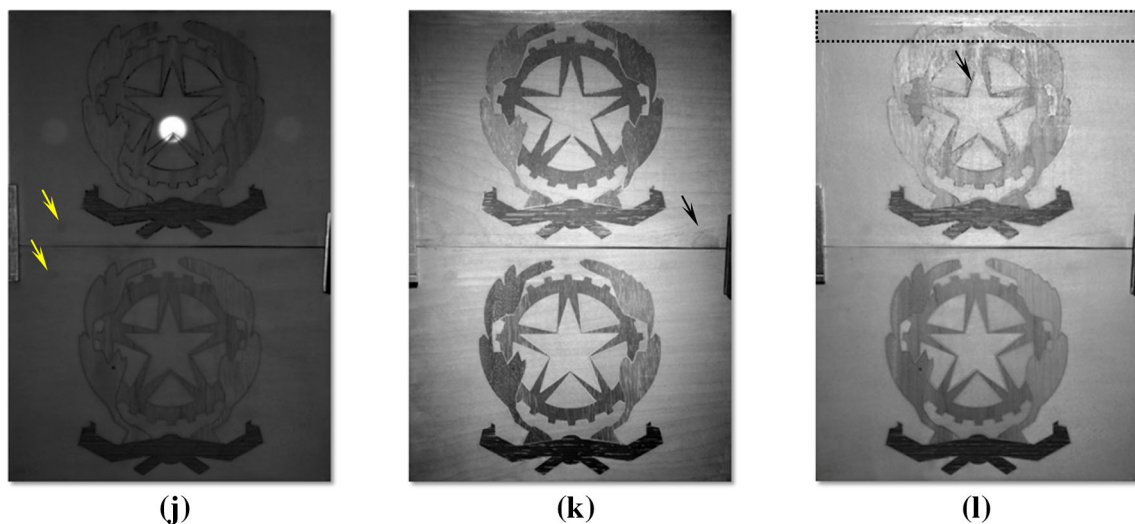


Fig. 20 continued

restorer. In particular, the sub-superficial voids, the wood grain or the wooden texture, insert of foreign and unwanted materials, the quality of the manufacture process via laser cutting can be studied by the proposed method.

Particular attention was given to the thermal stress applied during the inspection in the long-infrared region. Indeed, after a sound mechanical and thermal knowledge of the materials used in the construction of the samples, an ad hoc Matlab[®] script was realized [42] in order to establish—also thanks to the use of numerical simulations performed through Comsol Multiphysics[®] computer program—the optimal heat flux to be applied on the front or the rear side. The variation in temperature for the artwork to be restored is, in fact, a concern of the restorers. The numerical simulation [43] can be considered, at least for the method proposed in order to built the 3D geometry of the defective sample, as an interesting novelty in the scientific panorama.

An intriguing idea for the future, will be to apply the proposed method on a real case of *opus sectile*, which could be considered as close to the present. In order to provoke a thermal variation into the volume, the use of a source of vibrations instead of lamps can also be explored. Indeed, the *opus sectile* is an art technique popularized in the ancient and medieval Roman world, where materials were cut and inlaid into walls and floors to make a picture or pattern. Currently, this type of artwork is unexplored in the working at different wavelengths [44], as well as in the estimation of the emissivity variation [45]. The determination of the emissivity values per each type of wood were taken into account in the present research work in order to refine both the numerical simulation and, consequently, the experimental temperature deviations [46].

References

1. Hamilton Jackson, F.: Intarsia and marquetry—historical notes—antiquity. In: Curnow, R., Walsh, L., The Online Distributed Proofreading Team at <http://pgdp.net> (eds.) Handbooks for the Designer and Craftsman. William Hodge and Company, Glasgow (2009). <http://www.gutenberg.org/files/30215/30215-h/30215-h.htm>
2. Porter, B.: Timber. In: Rose, R. (ed.) Carpentry and Joinery 1. Butterworth Heinemann, Great Britain (2001). http://woodtools.nov.ru/books/carp_join/carp_join_1.pdf
3. Edwards, C.: Improving the decoration of furniture: imitation and mechanization in the marquetry process in Britain and America, 1850–1900. *Technol. Cult.* **53**(2), 401–434 (2012). doi:[10.1353/tech.2012.0073](https://doi.org/10.1353/tech.2012.0073)
4. Triboulot, M.C., Lavigne, E., Monteau, L., Boucher, N., Pizzi, A., Tekely, P.: The restoration of old wood furniture marquetry: protein glues, their analysis, upgrading and rehydration. *Holzforsch. Holzverwert.* **48**(4), 61–65 (1996). doi:[10.1016/j.indcrop.2015.02.030](https://doi.org/10.1016/j.indcrop.2015.02.030)
5. Ruzinska, E., Jabłonski, M.: Experimental model equipment for effective evaluation quality surface treatment of wooden materials. *Ann. Warsaw Univ. Life Sci. SGGW For. Wood Technol.* **70**, 259–263 (2010)
6. Ruffinato, F., Cremonini, C., Macchioni, N., Zanuttini, R.: Application of reflected light microscopy for non-invasive wood identification of marquetry furniture and small wood carvings. *J. Cult. Herit.* **15**(6), 614–620 (2014). doi:[10.1163/22941932-90000026](https://doi.org/10.1163/22941932-90000026)
7. Luxford, N., Strlic, M., Thickett, D.: Safe display parameters for veneer and marquetry objects: a review of the available information for wooden collections. *Stud. Conserv.* **58**(1), 1–12 (2013). doi:[10.1179/2047058412Y](https://doi.org/10.1179/2047058412Y)
8. Huber, J.: Conservation in focus: true colours revealed. *Icon News* **48**, 30–32 (2013). http://issuu.com/wallacecollection/docs/wallace_collection_whats_on_sep_nov
9. Sfarra, S., Theodorakeas, P., Avdelidis, N.P., Kouli, M.: Thermographic, ultrasonic and optical methods: a new dimension in veneered wood diagnostics. *Russ. J. Nondestruct.* **49**(4), 234–250 (2013). doi:[10.1134/S1061830913040062](https://doi.org/10.1134/S1061830913040062)
10. Radovanovic, M., Madic, M.: Experimental investigations of CO₂ laser cut quality: a review. *Nonconv. Technol. Rev.* **4**, 35–42 (2011). <http://www.revtn.ro/pdf4-2011/07%20-%20Radovanovic%20-%>

- 20Experimental%20Investigations%20Of%20CO2%20Laser%20Cut%20Quality.pdf
11. Cernecky, J., Bozek, P., Pivarciova, E.: A new system for measuring the deflection of the beam with the support of digital holographic interferometry. *J. Electr. Eng.* **66**(1), 53–56 (2015)
 12. Kreis, T.: Optical foundations of holography. In: Kreis, T. (ed.) *Handbook of Holographic Interferometry—Optical and Digital Methods*. Wiley-VCH, Weinheim (2005)
 13. Sfarra, S., Ibarra-Castanedo, C., Ambrosini, D., Paoletti, D., Bendada, A., Maldague, X.: Integrated approach between pulsed thermography, near-infrared reflectography and sandwich holography for wooden panel paintings advanced monitoring. *Russ. J. Nondestruct.* **47**(4), 284–293 (2011). doi:[10.1134/S1061830911040097](https://doi.org/10.1134/S1061830911040097)
 14. Sfarra, S., Theodorakeas, P., Ibarra-Castanedo, C., Avdelidis, N.P., Paoletti, A., Paoletti, D., Hrissagis, K., Bendada, A., Kouï, M., Maldague, X.: Evaluation of defects in panel paintings using infrared, optical and ultrasonic techniques. *Insight* **54**(1), 21–27 (2012). doi:[10.1784/insi.2012.54.1.21](https://doi.org/10.1784/insi.2012.54.1.21)
 15. Sfarra, S., Ibarra-Castanedo, C., Ridolfi, S., Cerichelli, G., Ambrosini, D., Paoletti, D., Maldague, X.: Holographic interferometry (HI), infrared vision and X-ray fluorescence (XRF) spectroscopy for the assessment of painted wooden statues: a new integrated approach. *Appl. Phys. A* **115**(3), 1041–1056 (2014). doi:[10.1007/s00339-013-7939-1](https://doi.org/10.1007/s00339-013-7939-1)
 16. Vest, C.M.: *Holographic Interferometry*. Wiley, New York (1979)
 17. Carslaw, H.S., Jaeger, J.C.: *General Theory*. Oxford University Press, N.Y. *Conduction of Heat in Solids* (1946)
 18. Isachenko, V., Osipova, V., Sukomel, A.: *Heat Transfer*. University Press of the Pacific, Honolulu (2000)
 19. López, G., Basterra, L.A., Acuña, L.: Estimation of wood density using infrared thermography. *Constr. Build. Mater.* **42**, 29–32 (2013). doi:[10.1016/j.conbuildmat.2013.01.001](https://doi.org/10.1016/j.conbuildmat.2013.01.001)
 20. Klein MT, Ibarra-Castanedo C, Maldague XP, Bendada A (2008) A straightforward graphical user interface for basic and advanced signal processing of thermographic infrared sequences. In: Vavilov, V.P., Burleigh, D.D. (eds.) *Proceedings of SPIE 6939. Thermosense XXX*, vol. 6939, Orlando. doi:[10.1117/12.776781](https://doi.org/10.1117/12.776781)
 21. Shepard, S.M., Lhota, J.R., Rubadeux, B.A., Ahmed, T., Wang, D.: Enhancement and reconstruction of thermographic NDT data. In: Maldague, X.P., Rozlosnik, A.E. (eds.) *Proceedings of SPIE, Thermosense XXIV*, vol. 4710. doi:[10.1117/12.459603](https://doi.org/10.1117/12.459603), Orlando (2002)
 22. Rajic, N.: Principal component thermography for flaw contrast enhancement and flaw depth characterization in composite structures. *Compos. Struct.* **58**(4), 521–528 (2002). doi:[10.1016/S0263-8223\(02\)00161-7](https://doi.org/10.1016/S0263-8223(02)00161-7)
 23. Senarathna, J., Rege, A., Li, N., Thakor, N.V.: Laser speckle contrast imaging: theory, instrumentation and applications. *IEEE Rev. Biomed. Eng.* **6**, 99–110 (2013). doi:[10.1109/RBME.2013.2243140](https://doi.org/10.1109/RBME.2013.2243140)
 24. Kirkpatrick, S.J., Duncan, D.D., Wanh, R.K., Hinds, M.T.: Quantitative temporal speckle contrast imaging for tissue mechanics. *J. Opt. Soc. Am. A* **24**(12), 3728–3734 (2007)
 25. Kirkpatrick, S.J., Duncan, D.D., Wells-Gray, E.M.: Detrimental effects of speckle-pixel size matching in laser speckle contrast imaging. *Opt. Lett.* **33**(24), 2886–2888 (2008)
 26. Boas, D.A., Dunn, A.K.: Laser speckle contrast imaging in biomedical optics. *J. Biomed. Opt.* **15**(1), 011109 (2010). doi:[10.1117/1.3285504](https://doi.org/10.1117/1.3285504)
 27. Nothdurft, R., Yao, G.: Imaging obscured subsurface inhomogeneity using laser speckle. *Opt. Express* **13**(25), 10034–10039 (2005)
 28. Sfarra, S., Theodorakeas, P., Ibarra-Castanedo, C., Avdelidis, N.P., Paoletti, A., Paoletti, D., Hrissagis, K., Bendada, A., Kouï M., Maldague, X.: Importance of integrated results of different non-destructive techniques to evaluate defects in panel paintings: the contribution of infrared, optical and ultrasonic techniques. In: *Proceedings of the SPIE 8084, O3A: Optics for Arts, Architecture and Archeology III*, Munich, Germany (2011)
 29. Cielo, P., Rousset, G., Bertrand, L.: Nondestructive interferometric detection of unbounded layers. *Opt. Laser Eng.* **5**, 231–248 (1984)
 30. Rousset, G., Bertrand, L., Cielo, P.: A pulsed thermoelastic analysis of photothermal surface displacements in layered materials. *J. Appl. Phys.* **57**, 4396–4405 (1985)
 31. Theodorakeas, P., Ibarra-Castanedo, C., Sfarra, S., Avdelidis, N.P., Kouï, M., Maldague, X., Paoletti, D., Ambrosini, D.: NDT inspection of plastered mosaics by means of transient thermography and holographic interferometry. *NDT&E Int.* **47**, 150–156 (2012)
 32. Ibarra-Castanedo, C., Sfarra, S., Ambrosini, D., Paoletti, D., Bendada, A., Maldague, X.: Diagnostics of panel paintings using holographic interferometry and pulsed thermography. *QIRT J.* **7**(1), 85–114 (2010)
 33. Forest Products Laboratory: *Wood Handbook—Wood as an Engineering Material*. General Technical Report FPL-GTR-190. U.S. Department of Agriculture, Forest Service, Forest Products Laboratory, Madison (2010)
 34. Beall, F.C.: Specific heat of wood. Research note FPL-0184. U.S. Department of Agriculture, Forest Service, Forest Products Laboratory, Madison (1968)
 35. Perilli, S., Regi, M., Sfarra, S., Nardi, I.: Comparative analysis of heat transfer for an advanced composite material used as insulation in the building field by means of Comsol Multiphysics and Matlabcomputer programs. *Rev. Rom. Mater.* **46**(2), 185–195 (2016)
 36. Onofrei, E., Codau, T.C., Petrusic, S., Bedek, G., Dupont, D., Soulat, D.: Analysis of moisture evaporation from underwear designed for fire-fighters. *AUTEX Res. J.* **14**, 1–13 (2014)
 37. Lunkenheimer, P., Wehn, R., Schneider, U., Loidl, A.: Glassy aging dynamics. *Phys. Rev. Lett.* **95**, 055702 (2005)
 38. MacIsaac, D., Kanner, G., Anderson, G.: Basic physics of the incandescent lamp (lightbulb). *Phys. Teach.* **37**, 520–525 (1999)
 39. Petersen, K., Klocke, J.: Understanding the deterioration of paintings by microorganisms and insects. In: Stoner, J.H., Rushfield, B. (eds.) *The Conservation of Easel Paintings*. Routledge (Taylor & Francis Group), New York (2012)
 40. Schellmann Nanke, C.: Animal glues: a review of their key properties relevant to conservation. *Rev. Conserv.* **8**, 55–66 (2007)
 41. Sfarra, S., Ibarra-Castanedo, C., Lambiase, F., Paoletti, D., Di Ilio, A., Maldague, X.: From the experimental simulation to integrated non-destructive analysis by means of optical and infrared techniques: results compared. *Meas. Sci. Technol.* **23**, 115601 (2012). doi:[10.1088/0957-0233/23/11/115601](https://doi.org/10.1088/0957-0233/23/11/115601)
 42. Sfarra, S., Perilli, S., Paoletti, D., Ambrosini, D.: Ceramics and defects: infrared thermography and numerical simulations a wide-ranging view for quantitative analysis. *J. Therm. Anal. Calorim.* **123**, 43–62 (2015). doi:[10.1007/s10973-015-4974-5](https://doi.org/10.1007/s10973-015-4974-5)
 43. Theodorakeas, P., Avdelidis, N.P., Cheilakou, E., Kouï, M.: Quantitative analysis of plastered mosaics by means of active infrared thermography. *Constr. Build. Mater.* **73**, 417–425 (2014). doi:[10.1016/j.conbuildmat.2014.09.089](https://doi.org/10.1016/j.conbuildmat.2014.09.089)
 44. Sfarra, S., Ibarra-Castanedo, C., Ambrosini, D., Paoletti, D., Bendada, A., Maldague, X.: Discovering the defects in paintings using non-destructive testing (NDT) techniques and passing through measurements of deformation. *J. Nondestruct. Eval.* **33**, 358–383 (2014). doi:[10.1007/s10921-013-0223-7](https://doi.org/10.1007/s10921-013-0223-7)
 45. Avdelidis, N.P., Moropoulou, A.: Emissivity considerations in building thermography. *Energy Build.* **35**, 663–667 (2003)
 46. López, G., Basterra, L.A., Acuña, L., Casado, M.: Determination of the emissivity of wood for inspection by infrared thermography. *J. Nondestruct. Eval.* **32**, 172–176 (2013). doi:[10.1007/s10921-013-0170-3](https://doi.org/10.1007/s10921-013-0170-3)